THE GEOLOGICAL SOCIETY OF AMERICA®

Documenting Earthquake-Induced Liquefaction Using Satellite Remote Sensing Image Transformations

THOMAS OOMMEN[1]

Department of Geological Engineering, Michigan Technological University, 1400 Townsend Drive, Houghton, MI 49931

LAURIE G. BAISE

Department of Civil and Environmental Engineering, Tufts University, Medford MA 02155

RUDIGER GENS

Alaska Satellite Facility, Geophysical Institute, University of Alaska–Fairbanks, Fairbanks, AK 99775

ANUPMA PRAKASH

Geophysical Institute, University of Alaska–Fairbanks, Fairbanks, AK 99775

RAVI P. GUPTA

Department of Earth Sciences, Indian Institute of Technology, Roorkee 247667, India

Key Terms: ***Earthquake, Liquefaction, Remote Sensing, Bhuj***

ABSTRACT

Documenting earthquake-induced liquefaction effects is important to validate empirical liquefaction susceptibility models and to enhance our understanding of the liquefaction process. Currently, after an earthquake, field-based mapping of liquefaction can be sporadic and limited due to inaccessibility and lack of resources. Alternatively, researchers have used change detection with remotely sensed pre- and post-earthquake satellite images to map earthquake-induced effects. We hypothesize that as liquefaction occurs in saturated granular soils due to an increase in pore pressure, liquefaction-induced surface changes should be associated with increased moisture, and spectral bands/transformations that are sensitive to soil moisture can be used to identify these areas. We verify our hypothesis using change detection with pre- and post-earthquake thermal and tasseled cap wetness images derived from available Landsat 7 Enhanced Thematic Mapper Plus (ETM$^+$) for the 2001 Bhuj earthquake in India. The tasseled cap wetness image is directly related to the soil moisture content, whereas the thermal image is inversely related to it. The change detection of the tasseled cap transform wetness image helped to delineate earthquake-induced liquefaction areas that corroborated well with previous studies. The extent of liquefaction varied within and between geomorphological units, which we believe can be attributed to differences in the soil moisture retention capacity within and between the geomorphological units.

INTRODUCTION

Historically, liquefaction-related ground failures have caused extensive structural and lifeline damage around the world. Recent examples of these effects include the damage produced during the 2001 Bhuj, India, 2010 Haiti, and 2010 and 2011 New Zealand earthquakes. It is observed from these earthquakes that the occurrence of co-seismic liquefaction is restricted to areas that contain saturated, near-surface granular sediments. Documenting earthquake-induced liquefaction is important for developing case history data sets of liquefaction. Recent work by Oommen et al. (2011) has shown that the bias due to the difference in the ratio of the occurrence/non-occurrence of liquefaction between the data set and population can adversely affect the ability to develop accurate probabilistic liquefaction susceptibility models (Oommen and

[1]Corresponding author: phone: 906-487-2045, fax: 906-487-3371, email: toommen@mtu.edu.

Baise, 2010; Oommen et al., 2010). Thus, with improved and more complete liquefaction case history data sets, earthquake professionals will be able to refine existing empirical prediction methods and enhance their understanding of liquefaction processes.

Currently, after an earthquake, the damages induced by the earthquake are documented by reconnaissance teams (Rathje and Adams, 2008). However, large earthquakes such as the 2001 M7.7 Bhuj earthquake, which shook 70% of India, killed 20,000 people, and made 600,000 people homeless, pose a great challenge to field reconnaissance teams attempting to document the entire suite of liquefaction effects. These challenges are due to (1) inaccessibility of sites immediately after the earthquake, (2) the short life span of surface manifestations of liquefaction effects, (3) difficulty in mapping the areal extent of the failure, and (4) lack of resources.

Satellite remote sensing involves imaging the surface of Earth in various spectral bands at different spatial and temporal resolutions and can provide an unbiased record of events. Previous researchers have used pre- and post-earthquake images to map earthquake-induced effects (Gupta et al., 1995; Kohiyama and Yamazaki, 2005; Mansouri et al., 2005; Rathje et al., 2005; Huyck et al., 2006; Kayen et al., 2006; Rathje et al., 2006; and Eguchi et al., 2010). These images are often used to aid reconnaissance teams (Hisada et al., 2005; Huyck et al., 2005). The current approach of computer-based processing of these images to support reconnaissance efforts falls into two general categories: (1) use of pre- and post-earthquake data to identify change, and (2) use of only post-earthquake imagery to identify damage. The limitation of the former approach is that if ideal pre- to post-earthquake image pairs are unavailable, there is no quality measure of non-earthquake-induced changes (e.g., seasonal vegetation changes) for the final change detection map. The approach of thematic classification using only post-earthquake images needs sufficient training instances for the supervised classification. The training instances of liquefaction-induced surface effects are only obtained from field reconnaissance efforts. Therefore, neither approach sufficiently aids the field reconnaissance teams in rapidly documenting liquefaction-induced surface effects.

The objective of this research is to describe and verify the utility of satellite remote sensing for aiding reconnaissance teams in better identifying liquefaction-induced surface effects using spectral bands/transformations that are sensitive to soil moisture. We hypothesize that because liquefaction occurs in saturated granular soils due to increase in pore pressure, which often results in vertical flow of water, liquefaction-induced surface changes should have an associated increase in soil moisture with respect to similar surrounding non-liquefied regions. The increase in soil moisture affects the signature in spectral bands that are sensitive to it, such as thermal infrared (TIR) and shortwave infrared (SWIR) (Yusuf et al., 2001). Additionally, components from special transforms, such as the tasseled cap transform wetness component, could potentially be suitable for identifying areas that have undergone increases in soil moisture from earthquake-induced liquefaction. The tasseled cap transformation is a useful tool to convert the spectral reflectance to physical scene characteristics and was originally developed for understanding important phenomena of crop development in spectral space (Kauth and Thomas, 1976; Crist and Cicone, 1984). In this study, we use the tasseled cap transform component, which relates the spectral reflectance of Landsat data to surface wetness. We test our hypothesis using satellite imagery and with previous studies from the Kutch region, in the state of Gujarat, western India, for the 2001 Bhuj earthquake (Figure 1).

STUDY AREA

On 26 January 2001, the Kutch region experienced one of the most deadly earthquakes to strike India in its history. The epicenter of this intra-plate earthquake, known as the Bhuj earthquake, was ~400 km away from the boundary of the Indian plate and ~1,000 km away from the boundary of the Himalayan plate (Rastogi, 2004). The Kutch region forms a crucial geodynamic part of the western continental margin of the Indian subcontinent, and it is designated zone V (Figure 2) in the seismic zoning map of India, having the highest earthquake risk. The Indian Standard (IS) building code assigns a zone factor of 0.36 to the Kutch region, which indicates that the buildings in that zone must be designed for forces associated with a horizontal ground acceleration of 0.36*g*. It is evident from Figure 2 that Kutch is the only region in India outside the plate-boundary region of the Himalayas that is designated as zone V.

After the Bhuj earthquake, widespread appearances of water bodies, sand boils, and channels were reported by several reconnaissance teams and by local residents in the Kutch region. The Indian remote sensing satellite (IRS-1C) with its Wide Field Sensor (WiFS) acquired an image 90 minutes after the 2001 Bhuj earthquake (26 January, 8:46 a.m.). This image captured near-real-time effects of the earthquake. Reconnaissance teams identified some of these as liquefaction and cited that the accessibility to several regions of the affected area was poor, particularly

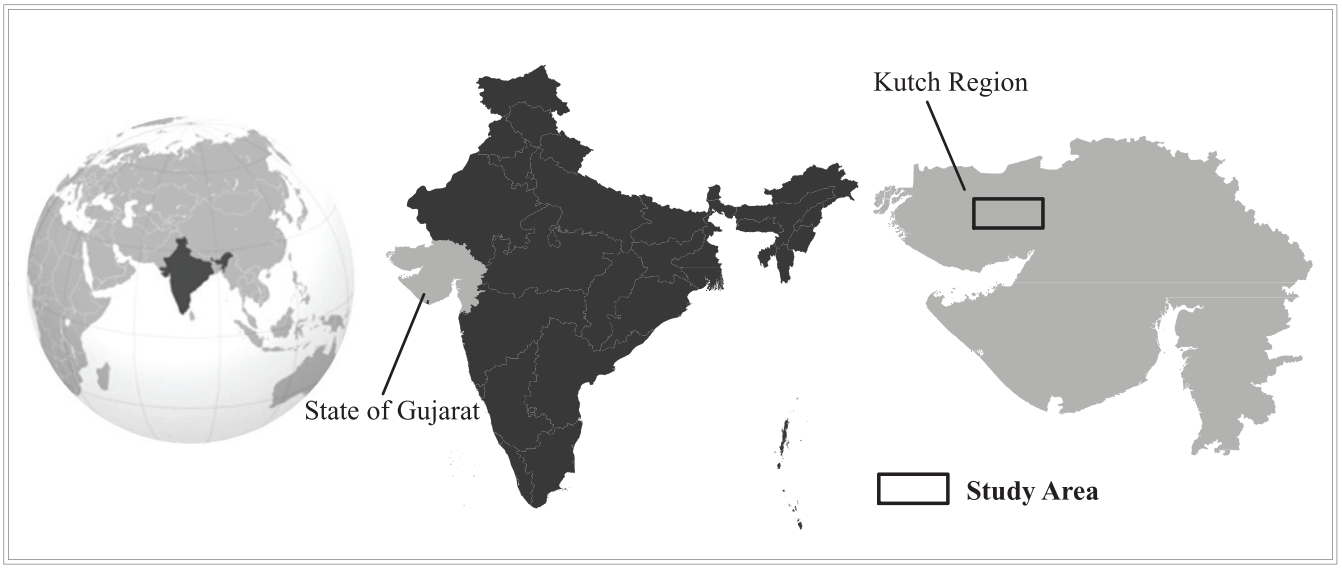

Figure 1. Study area map showing the Kutch region in the state of Gujarat in the western part of India.

due to earthquake-induced damage (Bilham, 2001; Mohanty et al., 2001; Narula and Choubey, 2001; Saraf et al., 2002; Singh et al., 2002; and Ramakrishnan et al., 2006). In this study, we use satellite images acquired by the National Aeronautics and Space Administration (NASA) Landsat Enhanced Thematic Mapper to evaluate its use in mapping earthquake-induced liquefaction-related surface effects.

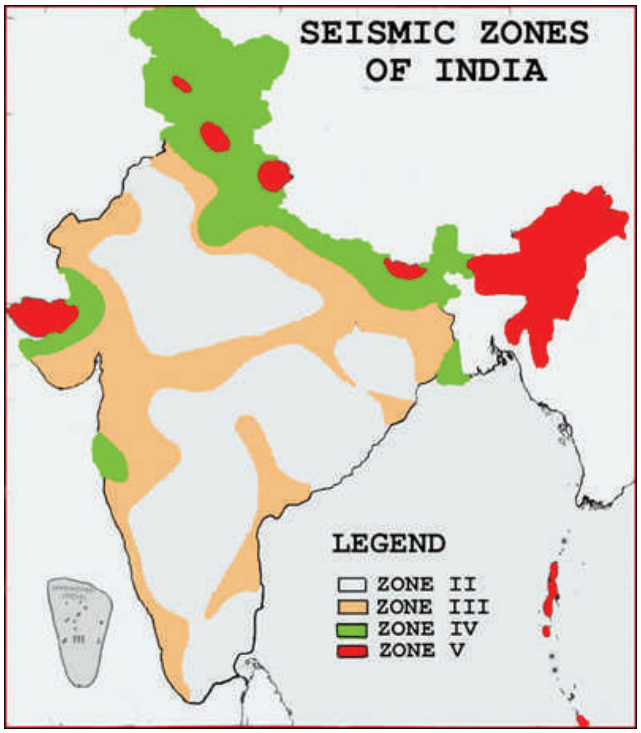

Figure 2. Seismic zoning map of India showing the distribution of the five different seismic zones across the country. Kutch (shown in rectangle) is the only region that is far from the Himalayan plate-boundary region and is still within the highest seismic risk (zone V). (Source: Institute of Seismological Research, Government of India.)

The study area (Kutch region) bears many geological similarities to the Mississippi Valley in the central United States, which contains the New Madrid Seismic Zone (Gomberg and Schweig, 2002). Lessons learned from the Bhuj earthquake can be readily applied to other areas such as the Mississippi Valley. Large damaging earthquakes are rare in intra-plate settings like Kutch and New Madrid, and, hence, each intra-plate earthquake provides a unique opportunity to make incremental advances in our ability to assess and understand the hazards posed by such events. Both of these regions have relatively flat topography, negating the need to correct the satellite data for varying local angle of incidence and varying backscattering behavior. Furthermore, the lack of vegetation in the Kutch region, as observed in the Normalized Difference Vegetation Index (NDVI) map (Figure 3), and the wealth of available data sets make it an ideal site to validate our hypothesis and establish the potential of satellite remote sensing for documenting the surface effects of earthquake-induced liquefaction.

DATA AND METHODOLOGY

In this study, we used two pre-earthquake and one post-earthquake Landsat ETM$^+$ images (Table 1). As a first step, atmospheric correction of image data was carried out using the Fast Line-of-Sight Atmospheric Analysis of Spectral Hypercubes (FLAASH) module

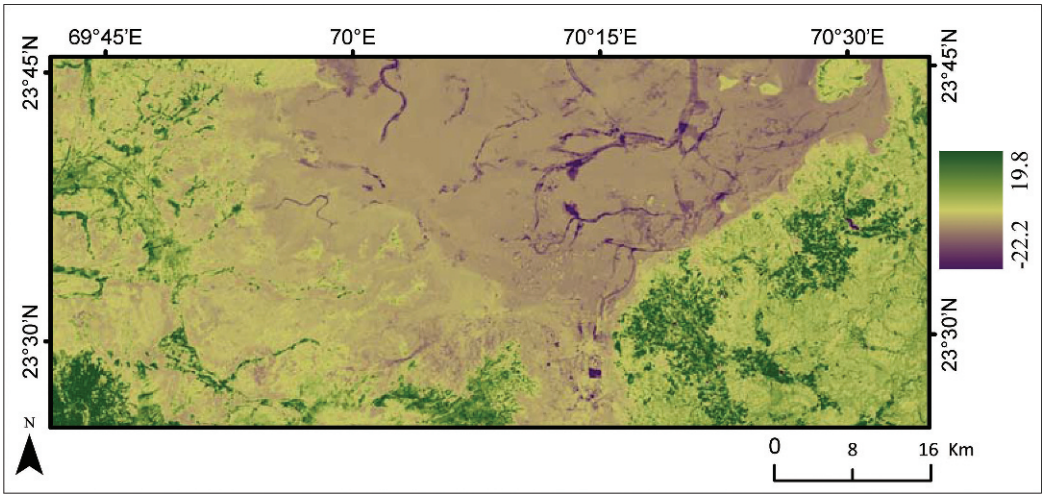

Figure 3. Normalized Difference Vegetation Index (NDVI) map of the study area developed using post-earthquake Landsat imagery. The NDVI values range from −22.2 to 19.8, with most of the region having values less than 0, indicating the absence of vegetation.

of the Environment for Visualizing Images (ENVI). All other data-processing steps were carried out using the Erdas Imagine software package. Field data for the study area were limited, at best. We used the tasseled cap transform wetness component of the Landsat image and the land surface temperature (LST) derived from the thermal band as a proxy for soil moisture. To map the change in soil moisture, we calculated the change in the tasseled cap transform wetness component between the pre- and post-earthquake images.

A direct change detection through subtraction of pre- and post-earthquake images captures changes due to the earthquake and other non-earthquake-related changes (e.g., seasonal changes). If the pre- and post-earthquake images are very closely spaced in time (difference on the order of days), the seasonal influence is disregarded, and the detected changes are attributed to the earthquake event. For the Bhuj earthquake, we had an ideally timed data set consisting of a January pre-earthquake image and a February post-earthquake image. Unfortunately, the January image was cloudy over large parts of the study area, and the effect of the cloud cover could not be completely removed through atmospheric correction and digital processing techniques. We therefore relied on the November pre-earthquake images for the change detection.

To determine the general magnitude of seasonal change between the November (pre-earthquake) and February (post-earthquake) times, we first checked the archived meteorological records (Weather Underground, 2012). Analyzing the temperature, precipitation, and wind data from November, December, January, and February for the years 2006 through 2011, we found that Bhuj, a desert area, witnesses a relatively monotonous warm dry winter weather pattern from November through February, with average monthly temperatures ranging from 20 to 25.55°C and no precipitation. Additionally, the area has little vegetation cover (Figure 3). Even with the vegetation cover that exists, the phenology of the vegetation sees a marked change only at the onset of summer (warm), onset of the rainy spell (wet), and onset of winter (cool). Once the winter sets in (in early November), the vegetation condition remains the same until late March–early April. In this study, it was reasonable to assume that the seasonal changes between November and February were minimal and much smaller in magnitude than the changes due to the earthquake event. Therefore, all results presented

Table 1. *Details of the available satellite data sets from the study area.*

Satellite/Sensor	Spectral Resolution (μm)	Band	Spatial Resolution (m)	Pre-Event Acquisition Date	Post-Event Acquisition Date
Landsat/ETM$^+$	0.45–0.9	VNIR: 4 bands	30	8 November 2000	9 February 2001
	1.55–2.35	SWIR: 2 bands	30		
	10.4–12.5	TIR: 1 band	60	8 January 2001	
	0.52–0.9	Pan: 1 band	15		

VNIR = visible and near infrared, SWIR = shortwave infrared, TIR = thermal infrared, PAN = panchromatic.

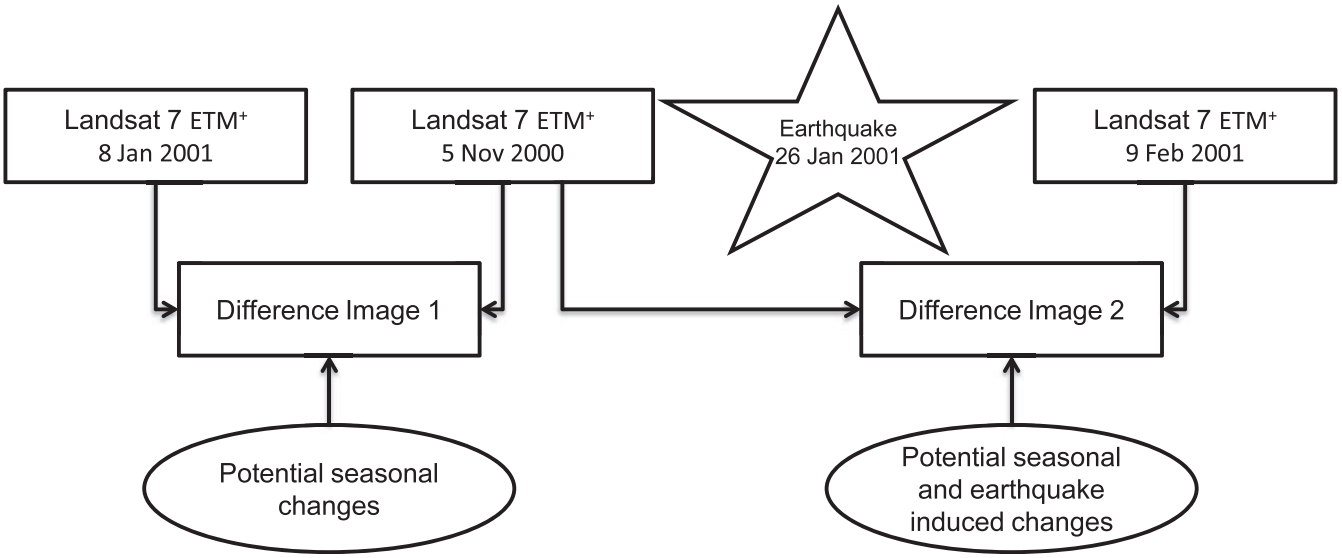

Figure 4. Schematic diagram to determine the magnitude of non-earthquake-related/seasonal change when using a pre- and post-earthquake image pair that has a large time difference. This processing was carried out on a subset of the image that was cloud free. Change detection results should be carefully interpreted in light of the information contained in the difference image 1.

later in the paper are direct change detection between the November and February images.

We also investigated alternate means to determine the magnitude of seasonal effects in pre- to post-earthquake image pairs that were significantly apart in time (Figure 4). Fortunately, the January image that was very close in time to the post-earthquake image had some portions that were cloud free. We used these cloud-free portions of the image and generated a difference image (difference image 1 in Figure 4) that captured all seasonal changes. We generated this difference image using the raw images and the processed products such as the temperature and tasseled cap wetness images. Figure 5 shows the tasseled cap wetness difference between the pre-earthquake image sets of November and January. The uniform color in this figure confirms that the seasonal effects are relatively uniform spatially. Moreover, the mean difference in wetness based on the image statistics is −0.02, and the standard deviation (std. dev.) is 0.05, which indicates that the change in wetness between the pre-earthquake dates is statistically insignificant. It is also safe to assume that these seasonal differences determined in the cloud-free area are representative for the entire study area under consideration. This analysis increased our confidence in relying on the November-February image pairs for further determining changes caused by the earthquake event. Information on the magnitude of seasonal change (Figure 5) is an important quality parameter, especially when reporting change detection results based on images with a relatively large time difference on the order of months.

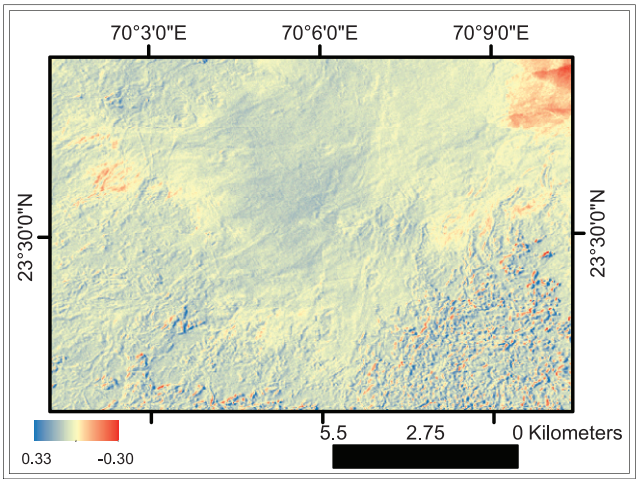

Figure 5. Influence of seasonal changes verified using the schematic in Figure 4 showing the difference between November and January tasseled cap wetness images (difference image 1 in Figure 4).

Finally, the changes mapped using the Landsat ETM$^+$ tasseled cap transform wetness image and the thermal image data set were compared and validated with the liquefaction instances reported by Singh et al. (2002) after the 2001 Bhuj earthquake. These instances were reported by Singh et al. (2002) by extensive field work and band rationing of pre- and post- earthquake images of Indian Remote Sensing satellite-ID-LISS-III.

Digital Number to Radiance

The use of satellite remote sensing to map objects or features on the surface of Earth is based on the

concept that different objects reflect energy differently in various parts of the electromagnetic spectrum. On a satellite image, this reflected energy is represented as a Digital Number (DN). The DN depends upon the calibration parameters and radiometric resolution of the satellite sensors. The optimum detection of objects in an image requires that the data be expressed in physical units, such as radiance or reflectance, where radiance is the amount of light (or other electromagnetic radiation) that the sensor ''sees'' from the object it is observing (Pandya et al., 2002; Srinivasulu and Kulkarni, 2003). Radiance has units of watts/square meter/steradian. Reflectance has no units and is the ratio of the intensity of light reflected by a target to that incident on it.

The DN values of the Landsat ETM$^+$ sensors were converted to spectral radiance using the following equation from Chander et al. (2009):

$$L_\lambda = L_{min\lambda} + \frac{L_{max\lambda} - L_{min\lambda}}{Q_{calmax}} Q_{cal}, \quad (1)$$

where L_λ is the spectral radiance, $L_{min\lambda}$ and $L_{max\lambda}$ are the minimum and maximum spectral radiance values of the satellite sensor corresponding to the gain settings at the time of acquisition, Q_{calmax} is the maximum possible DN value, which is 255 for the Landsat ETM$^+$ sensors, and Q_{cal} is the calibrated DN. The study area has generally low slope and flat topography, and therefore no topographic correction is necessary.

Atmospheric Correction

The nature of satellite remote sensing requires that the electromagnetic radiation passes through the atmosphere before being collected by the sensor on the satellite. As a result, these remotely sensed data include information of both the Earth's surface and the atmosphere. To quantitatively analyze the reflectance from the Earth's surface, an important preprocessing step is to compensate for atmospheric effects such as the amount of water vapor, distribution of aerosols, and scene visibility.

In this study, we use the FLAASH module for atmospheric correction of the Landsat ETM$^+$ bands 1–5 and 7 (Adler-Golden et al., 1999; Matthew et al., 2000). FLAASH uses the standard equation for spectral radiance given as:

$$L = \left(\frac{A\rho}{1-\rho_e S}\right) + \left(\frac{B\rho_e}{1-\rho_e S}\right) + L_a, \quad (2)$$

where L is the at-satellite sensor radiance, ρ is the surface reflectance of the pixel, ρ_e is the average surface reflectance for the pixel in the surrounding region, S is the spherical albedo of the atmosphere, L_a is the radiance backscattered by the atmosphere, and A and B are coefficients that relate to atmospheric and geometric conditions of the site. The values of ρ and ρ_e depend upon the wavelength of the spectral channel and account for the spatial mixing of radiance among nearby pixels caused by atmospheric scattering. FLAASH determines the values of A, B, S, and L_a from the MODerate resolution atmospheric TRANsmission (MODTRAN4) calculations, which use the satellite viewing angle, solar angle, mean surface elevation, aerosol type, visible range, and an atmospheric model based on the site (Felde et al., 2003).

FLAASH computes the spatial-averaged pixel radiance using a point-spread function that describes the relative contributions to the pixel radiance from points on the ground at different distances from the direct line of sight. It also retrieves the aerosol amount by iterating over large visible ranges.

The scene and sensor information needed for the atmospheric correction was obtained from the header file of the Landsat ETM$^+$ image. The tropical atmospheric model for the MODTRAN4 calculation was selected based on the latitude of the study area. An initial visibility of 40 km was assumed for the images, which represents clear sky conditions for the retrieval of the aerosol corrections. FLAASH converts the spectral radiance to at-surface reflectance.

Radiance to Temperature

The energy emitted from Earth's surface in the thermal infrared spectrum (3–15 μm) enables us to calculate the radiant temperature using Planck's law. In the past, researchers have analyzed the applicability of satellite-derived surficial temperature for studying both surficial and sub-surficial characteristics (Prakash et al., 1995; Saraf et al., 1995; Prakash and Gupta, 1999; and Zhang et al., 2004). We use the pre- and post-event Landsat ETM$^+$ band-6 image to calculate the top of the atmosphere (pre-atmospheric correction) radiant temperature for the study area. Further, the Landsat ETM$^+$ measured spectral radiance is converted to the temperature using Planck's radiation equation:

$$T = \frac{C_2}{\lambda \ln\left[\left(\tau_\lambda \varepsilon_\lambda C_1 \lambda^{-5}/\pi L_\lambda\right) + 1\right]}, \quad (3)$$

where $C_1 = 2\pi hc$, $C_2 = hc/k$, L_λ is the spectral radiance in W m^{-2} ster^{-1} μm^{-1}, h is Planck's constant (6.626×10^{-34}js), k is Boltzmann's constant (1.380×10^{-23} JK^{-1}), T is temperature in K, c is the speed of light

Table 2. *Tasseled cap coefficients for Landsat ETM$^+$ at-satellite reflectance (source: Huang et al., 2002).*

Index	Band 1	Band 2	Band 3	Band 4	Band 5	Band 7
Brightness	0.3561	0.3972	0.3904	0.6966	0.2286	0.1596
Greenness	−0.3344	−0.3544	−0.4556	0.6966	−0.0242	−0.2630
Wetness	0.2626	0.2141	0.0926	0.0656	−0.7629	−0.5388
Fourth	0.0805	−0.0498	0.1950	−0.1327	0.5752	−0.7775
Fifth	−0.7252	−0.0202	0.6683	0.0631	−0.1494	−0.0274
Sixth	0.4000	−0.8172	0.3832	0.0602	−0.1095	0.0985

(2.998×10^8 ms^{-1}), τ_λ is the atmospheric transmittance, and ε_λ is the spectral emissivity.

Equation 3 can be simplified for Landsat ETM$^+$ as:

$$T = \frac{K_2}{ln\left(\frac{K_1}{L_\lambda} + 1\right)} - 273, \tag{4}$$

where $K_1 = 666.09$ W m^{-2} $ster^{-1}$ μm^{-1}, $K_2 = 1260.56$ K, and T is the temperature in °C (Chander et al., 2009).

Land surface temperature (LST) is a valuable diagnostic of soil moisture measurement because soil surface temperature increases with decreasing soil water content (less evaporative cooling), while moisture depletion in the plant root zone results in stomatal closure, reduced transpiration, and elevated canopy temperatures (Anderson et al., 2007; Eltahir, 1998; and Vicente-Serrano et al., 2004). Shih and Jordan (1993) found a coefficient of correlation (r) of 0.84 between LST and soil moisture content.

Tasseled Cap Transformation

In this study, we use the tasseled cap transformation coefficients for Landsat ETM$^+$ reflectance developed by Huang et al. (2002) (Table 2). Huang et al. (2002) developed this transformation using several-hundred field observations of soil, impervious surfaces, dense vegetation, and moisture content. The field data were used to determine the rotation of the principal axes obtained from principal component analysis (PCA) by preserving its orthogonality. The technique utilizes a Gram-Schmidt sequential orthogonal transformation (Huang et al., 2002). The difference between tasseled cap and PCA is that while PCA places an *a priori* order on the principal directions in the data, the Gram-Schmidt approach allows the user to choose the order of the calculation based on a physical interpretation of the image. This transformation converts the Landsat ETM$^+$ band (bands 1–5, 7) reflectance into six axes, of which three major axes correspond to physical characteristics such as brightness, greenness, and wetness. We make use of the Landsat ETM$^+$ image tasseled cap transform wetness axes to evaluate the increase in surface wetness/moisture content between the pre- and post-earthquake coverage.

Change Detection

An important application of satellite remote sensing data is to detect changes occurring on the surface of Earth. Change detection methods can be categorized broadly as either supervised or unsupervised according to the nature of the data-processing technique applied (Lu et al., 2004). Supervised change detection is based on a supervised classification method, which requires the availability of a ground truth in order to derive a suitable training set for the learning process of the classifier, whereas the unsupervised change detection approach performs change detection by making a direct comparison of the pre- and post-earthquake images. Unsupervised change detection is mainly carried out using one of the following: (1) image differencing, (2) image ratioing, (3) change vector analysis, or (4) PCA. These change detection techniques have been reviewed by several researchers (Singh, 1989; Mouat et al., 1993; Deer, 1995; Coppin and Bauer, 1996; Jensen et al., 1997; Prakash and Gupta, 1998; Serpico and Bruzzone, 1999; and Yuan et al., 1999). In this study, the unsupervised change detection is performed by image differencing as follows:

$$D(x) = I_2(x) - I_1(x), \tag{5}$$

where $D(x)$ is the difference image, $I_2(x)$ is the post-earthquake image, and $I_1(x)$ is the pre-earthquake image. The image differencing results in positive and negative values in areas of surface change and near-zero values in areas of no change. The difference image often produces a distribution that is approximately Gaussian in nature, with pixels of no change distributed around the mean and changed pixels distributed in the tails of the distribution (Gupta, 2003). A necessary pre-processing step before image differencing is normalization or standardization to reduce the inherent variability between the multi-temporal data sets (pre- and post-earthquake image) (Warner and Chen, 2001). In this study, image standardization is applied before image differencing. A change class map was developed from

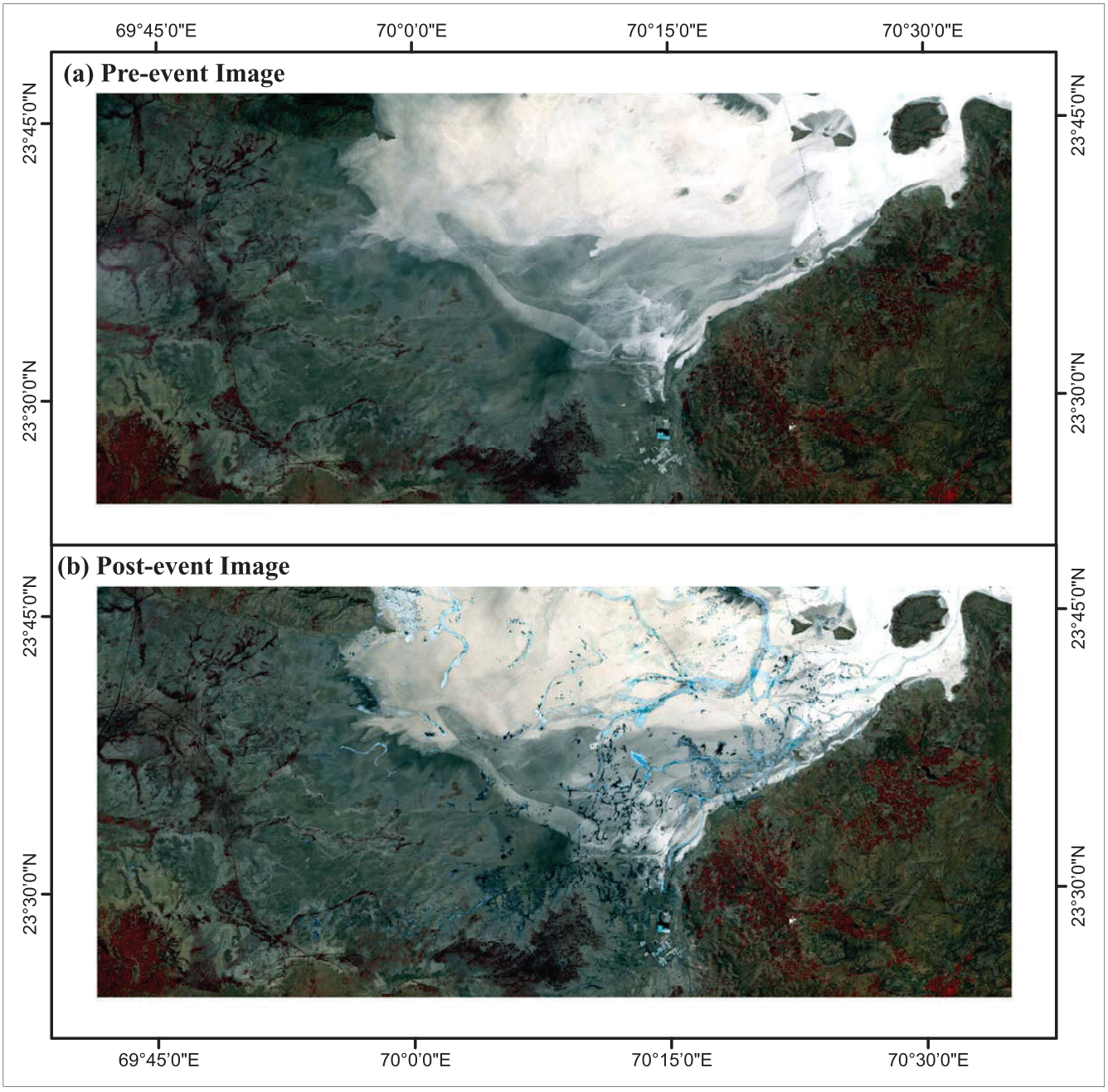

Figure 6. Comparison of Landsat ETM$^+$ pre- and post-earthquake images: (a) standard false color composite of the pre-earthquake (8 January 2001) image, and (b) standard false color composite of the post-earthquake (9 February 2001) image. The vegetation is seen as red.

the difference image by simply thresholding it according to the following decision rule:

$$B(x) = \begin{cases} 1, & if\,|D(x)| > \tau \\ 0, & otherwise \end{cases}, \qquad (6)$$

where $B(x)$ denotes the change map, and τ denotes the threshold. The minimum number of change classes in a change map is two (i.e., positive and negative change classes). In this study, we used 11 change classes with five positive change classes, five negative change classes, and one no-change class, with the thresholds being evenly spaced between -1 and $+1$.

ANALYSIS RESULTS AND DISCUSSION

A Landsat ETM$^+$ pre- and post-earthquake standard false color composite (Figure 6) shows that the

study area has little vegetation and a generally flat topography. The vegetated areas (red tones in Figure 6) are mostly towards the southeast, southwest, and western corners of the study area, and the NDVI image confirms this observation (Figure 3). Even though the study area has mostly flat topography, Patel (1997) identified three major geomorphologic units in the area: (1) the Pre-Quaternary Outcrop, (2) the Banni Grassland, and (3) the Great Barren Zone. The Pre-Quaternary Outcrop and the Banni Grassland are composed of slightly elevated patches of grassland along with intervening channels and are mostly composed of fine micaceous sand and silt with clay intercalations (Rajendran and Rajendran, 2001). The Pre-Quaternary Outcrop and Banni Grassland are together referred as the ''bet'' zone (bet meaning ''slightly raised land'') in this study. The elevation difference between the bet zone and the Great Barren Zone is about 2–3 m (Rajendran and Rajendran, 2001).

The Great Barren Zone mostly consists of salty lowland that is seasonally marshy. The northern part of the study area, which is part of the Great Barren Zone, is adjacent to an inlet to the Arabian Sea that floods annually. When the saltwater from the flooding dries, a white salty crust is left behind (Gomberg and Schweig, 2002). The bright white signature observed towards the north of the study area in the Landsat ETM^+ pre- and post-earthquake standard false color composite image (Figure 6) demonstrates the presence of the salty crust. Several changes in the Great Barren Zone are visible between the pre- and post-earthquake images.

Figure 7 presents the tasseled cap wetness image for the pre- and post-earthquake dates obtained using the Landsat ETM^+ tasseled cap transform. In the pre-earthquake tasseled cap wetness image (Figure 7a), the difference in wetness between the Great Barren Zone and bet zone is distinct. In the post-earthquake tasseled cap wetness image (Figure 7b), several localized regions of increased wetness are observed in the Great Barren Zone. Figure 7c presents the difference image between the pre- and post-earthquake tasseled cap wetness images. The areas with increased wetness likely represent areas where the soil moisture content has increased. Figure 7d represents the areas of extreme increase in tasseled cap wetness, where extreme increase is defined as a change in wetness magnitude of $>+1.5$ standard deviation.

Figure 8 presents the computed LST for the pre- and post-earthquake dates using the Landsat ETM^+ images. The estimated temperature within the study area ranged from 23.5 to 44.5°C and 16.8 to 47.1°C for November and February images, respectively. The radiant temperatures are listed in Table 3. A comparison of the November pre-earthquake temperature image (Figure 8a) with the February post-earthquake temperature image (Figure 8b) shows that the bet zone is much warmer than the Great Barren Zone in both the pre- and post-earthquake images. These observations correspond with the wetness difference observed between the bet and Great Barren Zones in the pre- and post-earthquake tasseled cap wetness images (Figure 7).

It is evident from comparing the pre- (Figure 8a) and the post-earthquake (Figure 8b) images that pockets exist within the Great Barren Zone that have significant reductions in temperature compared to the surrounding areas. Figure 8c presents the difference image between the pre- and post-earthquake LST images. In Figure 8c, blue represents regions where the temperature has decreased, whereas brown represents regions where the temperature has increased in the post-earthquake image relative to the pre-earthquake image. Because the surface temperature is inversely related to the moisture content, the areas with decreased temperature could possibly represent areas of increased moisture content. Further, we filtered the areas that have extreme reduction/decrease in temperature (change in temperature <-1.5 standard deviation). These areas (represented in red) are shown in Figure 8d.

Figure 9 compares the extreme changes in radiant temperature and the tasseled cap wetness observed from the Landsat ETM^+ images with the liquefaction instances reported by Singh et al. (2002). Figures 9b and 9c show the overlay of the extreme radiant temperature and extreme wetness, respectively, on the mapped liquefaction instances. In Figure 9b, we find low correspondence between the extreme temperature changes and the liquefaction instances reported by Singh et al. (2002). Moreover, we also find several areas with extreme reductions in temperature that extend beyond the liquefaction instances reported by Singh et al. (2002). This might be explained by the coarser spatial resolution (60 m) of the temperature data. However, Figure 9c shows that extreme wetness changes correspond well with the liquefaction instances reported by Singh et al. (2002). This correspondence is best towards the center and the south of the study area, whereas the wetness change under-predicts the liquefaction instances towards the north.

The pre-earthquake tasseled cap wetness image (Figure 7a) shows that the surface moisture levels increased within the Great Barren Zone toward the northern part of the study area compared to the rest of the Great Barren Zone. The liquefaction instances reported by Singh et al. (2002) in the study area towards the south are in the bet zone, whereas the instances of liquefaction mapped in the northern part

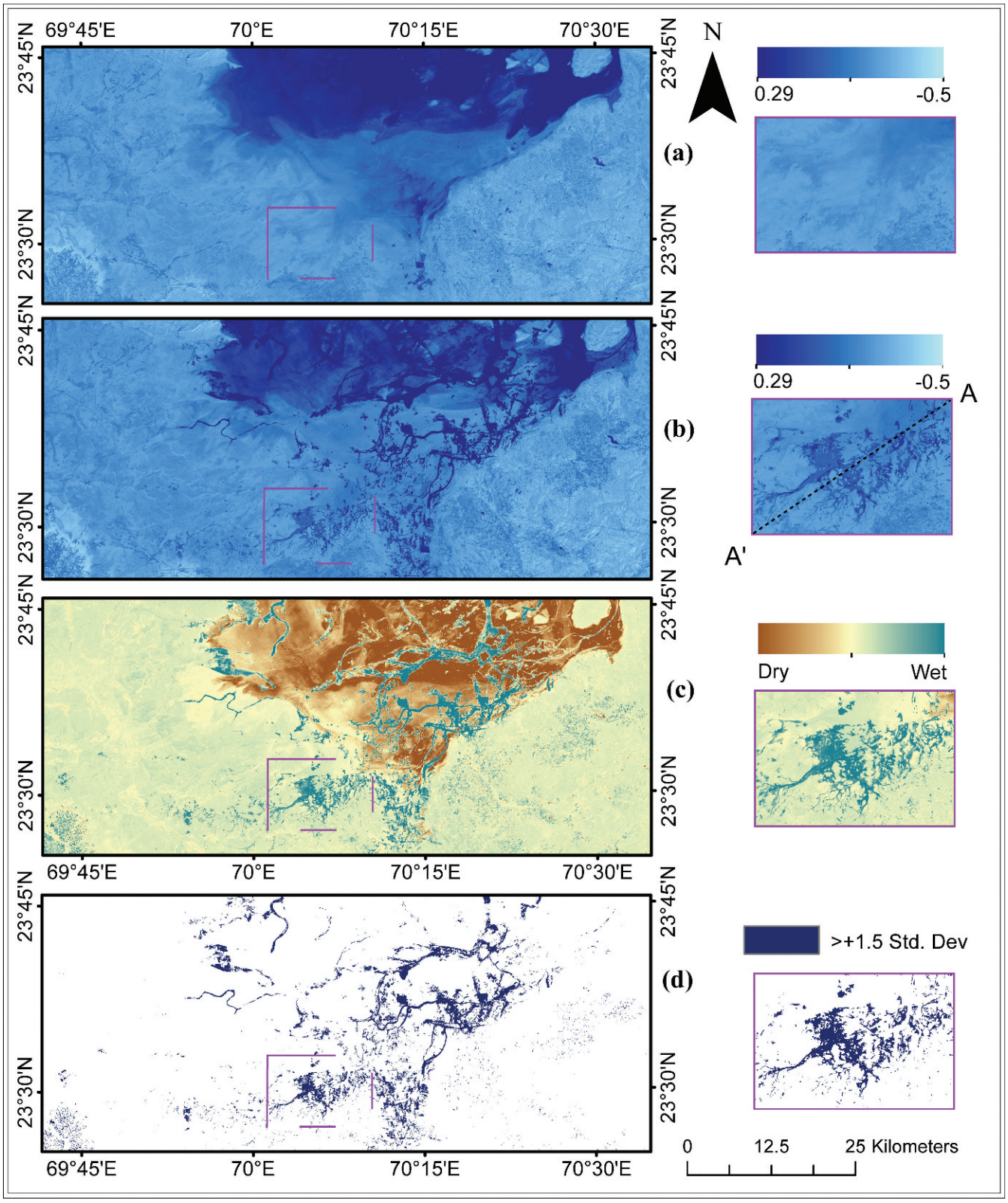

Figure 7. Landsat ETM$^+$ tasseled cap wetness: (a) pre-earthquake tasseled cap wetness image (November), (b) post-earthquake tasseled cap wetness image (February), (c) tasseled cap wetness difference image (February–November), and (d) locations with extreme increase in wetness (i.e., >+1.5 standard deviation filtered). Insets show the region within the study area.

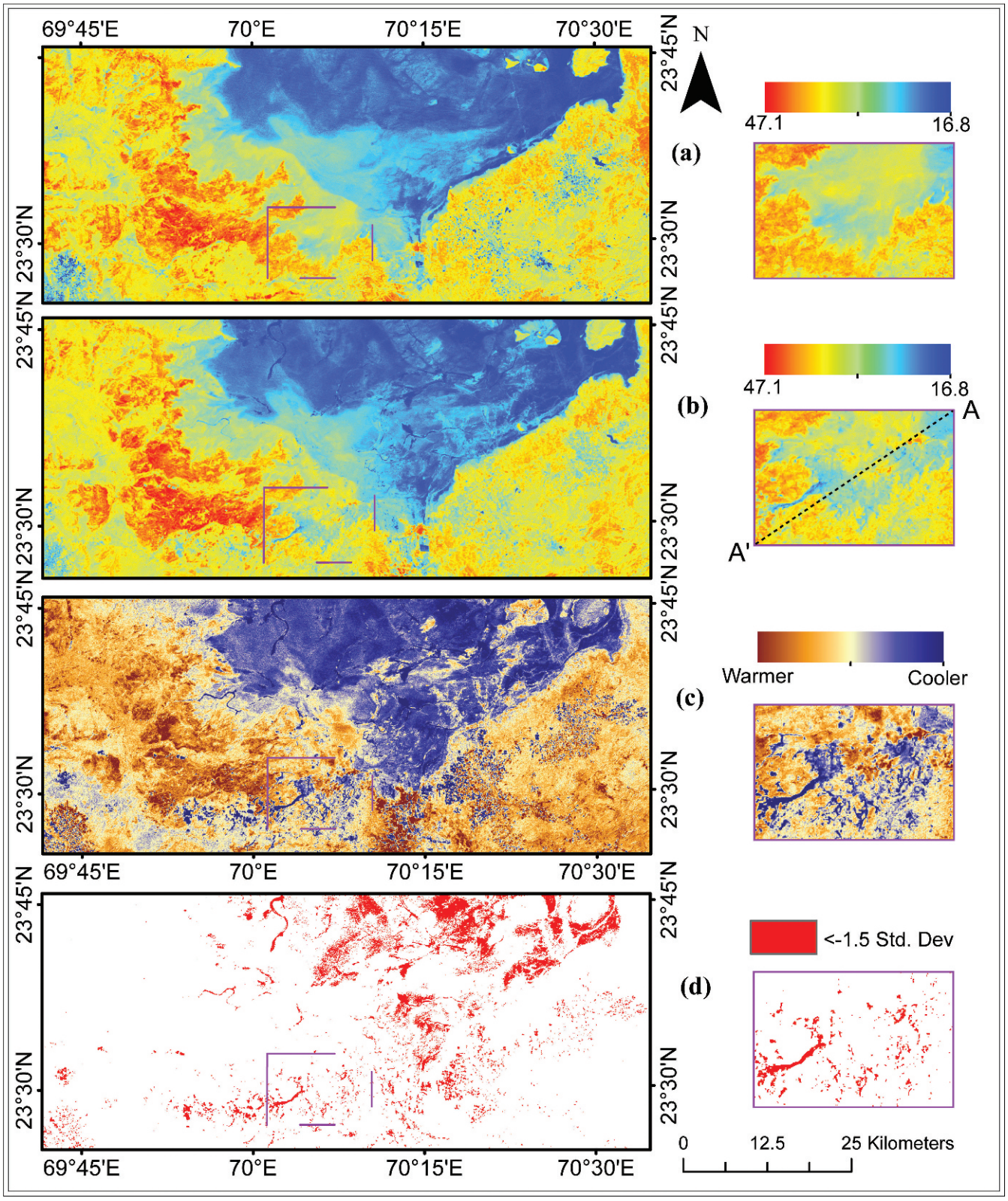

Figure 8. Landsat ETM$^+$ LST image in degree celsius (°C): (a) pre-earthquake LST image (November), (b) post-earthquake LST image (February), (c) LST difference image (February–November), and (d) locations with extreme reduction in temperature (i.e., <-1.5 standard deviation filtered). Insets show the region within the study area.

Table 3. *The computed ranges of radiant temperature (LST) from the various Landsat scenes.*

Date of Acquisition	Temperature Range (°C)	"Bet" Zone (°C)	Great Barren Zone (°C)
November 5, 2000	23.5–44.5	32.7–44.5	23.5–32.7
January 8, 2001	4.9–32.8	20.5–32.8	4.9–20.5
January 26, 2001		Earthquake event	
February 9, 2001	16.8–47.1	26.0–47.1	16.8–26.0

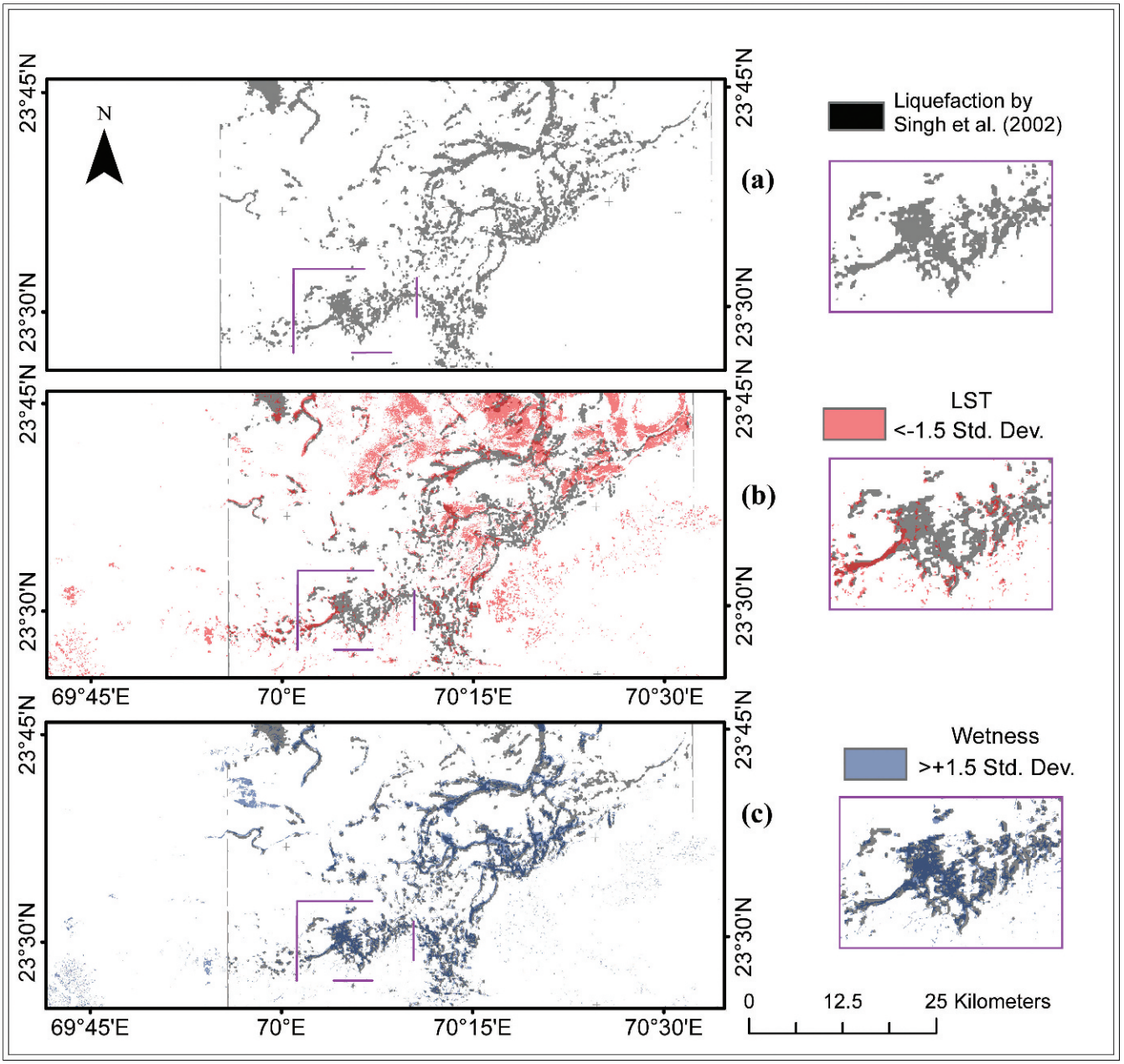

Figure 9. Extreme changes in temperature and tasseled cap wetness overlaid on liquefaction instances from 2001 Bhuj earthquake reported by Singh et al. (2002). (a) Liquefaction instances reported by Singh et al. (2002). (b) Overlay of extreme changes from radiant temperature image difference. (c) Overlay of extreme changes from tasseled cap wetness image difference. Insets show the region within the study area.

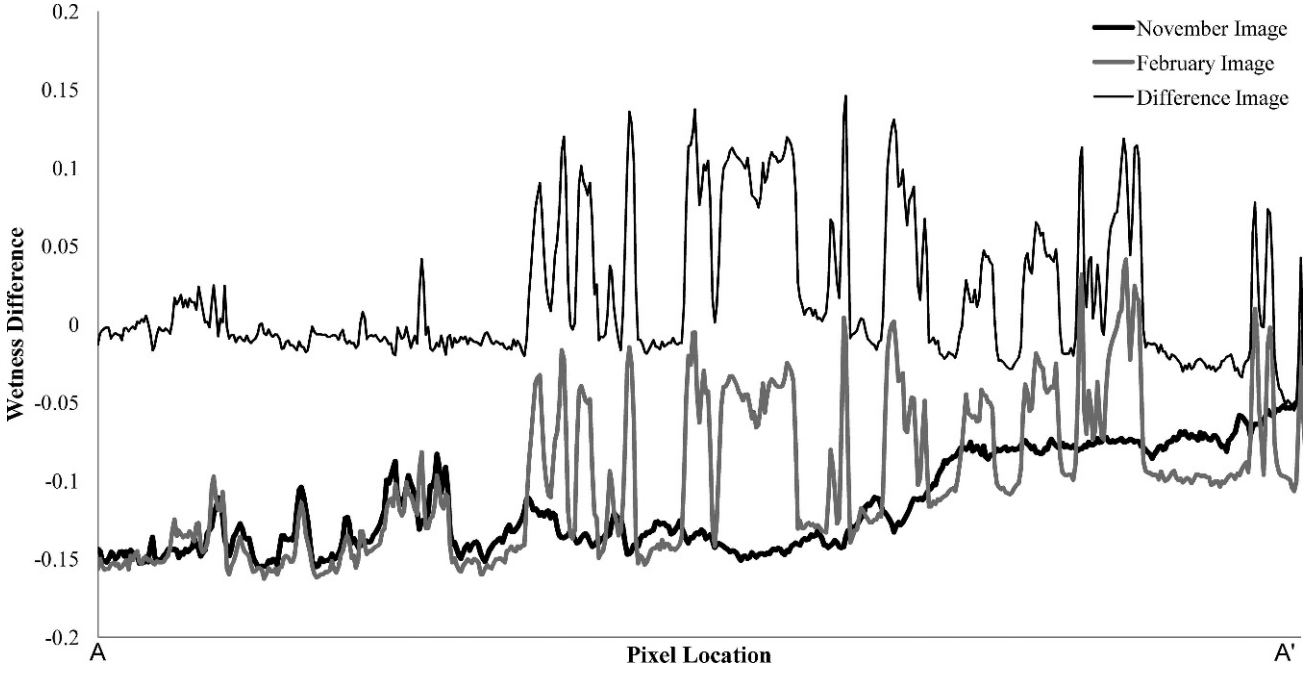

Figure 10. Landsat ETM$^+$ tasseled cap wetness difference profile along section A–A′ (profile line is shown in Figure 7b inset).

of the study area are in the Great Barren Zone. The reason why the liquefaction instances within the Great Barren Zone in the north are not identified well from the extreme changes is probably because the soil in the north is already wet, and the magnitude of change in wetness is smaller compared to the southern region. This could also be related to the soil retention capacity of the geomorphological units. Therefore, incorporating the pre-earthquake variability in moisture content and the variability in soil moisture retention capacity of the geomorphological units, and filtering the extreme changes based on these characteristics will be critical when using remote sensing to map earthquake-induced liquefaction.

Figure 10 presents profile A-A′ (location of profile line is shown in Figure 7b inset) along the pre- and post-earthquake tasseled cap wetness images and the difference image. The pre-earthquake tasseled cap wetness profile shows some variations in wetness from A to A′, with areas closer to A′ being wetter than those closer to A. A similar trend is seen on the pre-earthquake temperature image profile (Figure 11), with values closer to A′ being lower in temperature compared to values closer to A. The post-earthquake profile and the difference profile of tasseled cap wetness and thermal image capture the variation due to increased moisture content of surface soils. The variation in the thermal change profile is much more subtle than the tasseled cap wetness profile and is probably influenced by the coarser spatial resolution of the thermal image.

CONCLUSIONS

In this study, we evaluate the applicability of using changes in temperature and moisture content as detected from satellite remote sensing for mapping the surficial expression of earthquake-induced liquefaction. We hypothesize that because liquefaction occurs in saturated granular soils, the liquefaction-related surface changes should have an associated increase in soil moisture with respect to the surrounding non-liquefied regions. We test this hypothesis for the Bhuj region, where liquefaction was observed after the 2001 earthquake, using Landsat ETM$^+$ thermal and tasseled cap wetness transform image by image differencing of pre- and post-earthquake images. We further filter the extreme changes in the difference image and compare it with the liquefaction instances reported by Singh et al. (2002) by remote sensing and extensive fieldwork. We draw the following conclusions:

- The use of remotely sensed data that are sensitive to soil moisture can be an integral part in regionally documenting surface effects of earthquake-induced liquefaction and strategizing post-earthquake response and reconnaissance.
- The pre- and post-earthquake Landsat ETM$^+$ tasseled cap transform wetness difference image shows promise in mapping the surficial expression of earthquake-induced liquefaction and has a higher resolution than the thermal image (30 m versus 60 m).

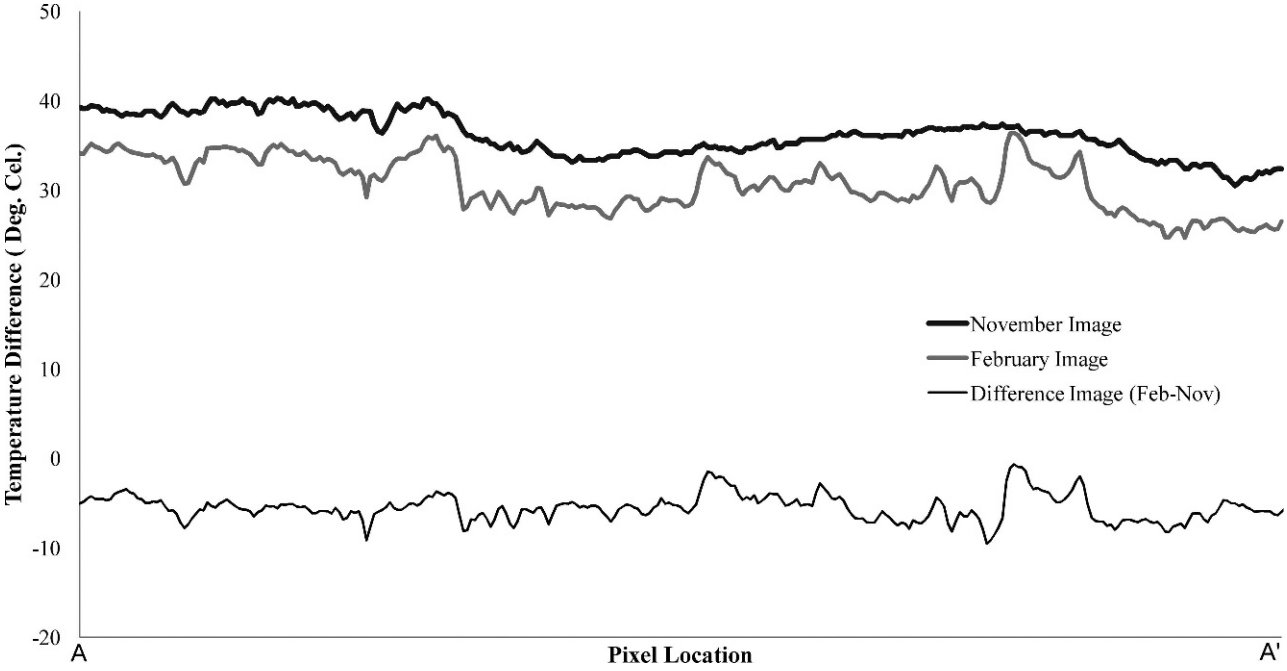

Figure 11. Landsat ETM$^+$ radiant temperature difference profile along section A-A′ (profile line is shown in Figure 8b inset).

- The correlation of the extreme changes filtered from the tasseled cap wetness image with liquefaction instances reported by Singh et al. (2002) verifies our hypothesis that the liquefaction zones have an associated increase in soil moisture with respect to the surrounding non-liquefied regions.
- Correlation of the changes mapped from tasseled cap wetness with liquefaction instances reported by Singh et al. (2002) was higher in the southern portion of the study area compared to the northern portion.
- The difference in the liquefaction instances mapped from the tasseled cap wetness change within and outside the Great Barren Zone indicates that the associated increase in soil moisture due to liquefaction is related to the soil moisture retention capacity of the geomorphological unit, and the inclusion of this factor could improve the mapping of liquefaction instances across the geomorphologic units.
- When using pre- to post-earthquake images that have a large difference in time, it is advisable to provide a quality measure for the magnitude of non-earthquake-induced changes (e.g., seasonal changes), where possible.
- The image difference of the pre- and post-earthquake Landsat ETM$^+$ thermal band image indicates that its spatial resolution limits its application for detailed mapping of liquefaction effects. The thermal images identify larger liquefaction features but not the numerous smaller features.

An obvious limitation for this approach to mapping of liquefaction is that meteorological factors, such as a heavy rain event prior to the post-earthquake image acquisition, would suppress surficial expressions of liquefaction. The available pre- to post-earthquake images that we used to ascertain the seasonal effects were taken two months apart. Even though the general weather conditions and phenology in Bhuj area remained largely comparable, there were some temporal changes. The current study area does not have high topographic relief nor dense vegetation. Studies should verify the applicability of this approach in areas of varying topography and vegetation. Furthermore, the moisture retention capacity of geomorphological units and their initial moisture condition should be incorporated to improve the estimates of the extent of liquefaction effects.

DATA AND RESOURCES

The Landsat data sets for this study were obtained from the U.S. Geological Survey site http://glovis.usgs.gov (last accessed on October 2011). These publications were also accessed online: Bilham (2001) http://cires.colorado.edu/~bilham/Gujarat2001.html (last accessed on October 2011), Mohanty et al. (2001) http://www.gisdevelopment.net/ (last accessed on October 2011), and Narula and Choubey (2001) http://www.iitk.ac.in/nicee/EQ_Reports/Bhuj/narula1.htm (last accessed on October 2011).

ACKNOWLEDGMENTS

This research was supported by the U.S. Geological Survey, Department of the Interior, National Earthquake Hazards Reduction Program (NEHRP) through awards G10AP00025 and G10AP00026. The views and conclusions contained in this document are those of the authors and should not be interpreted as necessarily representing the official policies, either expressed or implied, of the U.S. government. The authors sincerely thank Drs. Jeff Keaton, Charles M. Brankman, and the unknown reviewer for their constructive comments and suggestions.

REFERENCES

Adler-Golden, S. M.; Matthew, M. W.; Bernstein, L. S.; Levine, R. Y.; Berk, A.; Richtsmeier, S. C.; Acharya, P. K.; Anderson, G. P.; Felde, G. W.; Gardner, J.; Hoke, M. P.; Jeong, L. S.; Pukall, B.; Mello, J.; Ratkowski, A.; and Burke, H. H., 1999. Atmospheric Correction for Short-Wave Spectral Imagery Based on MODTRAN4. *Society of Photo-optical Instrumentation Engineers (SPIE) Proceeding, Imaging Spectrometry*, Vol. 3753, pp. 61–69.

Anderson, M.; Norman, J.; Mecikalski, J.; Otkin, J.; and Kustas, W., 2007, A climatological study of evapotranspiration and moisture stress across the continental U.S. based on thermal remote sensing: *Journal of Geophysical Research*, Vol. 112, D10117, doi: 10.1029/2006JD007506.

Bilham, R., 2001, *26 January 2001 Bhuj earthquake, Gujarat, India*: Electronic document, available at http://cires.colorado.edu/~bilham/Gujarat2001.html

Chander, G.; Markham, B.; and Helder, D., 2009, Summary of current radiometric calibration coefficients for Landsat MSS, TM, ETM+, and EO-1 ALI sensors: *Remote Sensing of Environment*, Vol. 113, No. 5, pp. 893–903.

Coppin, P. and Bauer, M., 1996, Digital change detection in forest ecosystem with remote sensing imagery: *Remote Sensing of Environment*, Vol. 13, pp. 207–234.

Crist, E. P. and Cicone, R. C., 1984, A physically-based transformation of Thematic Mapper data—The TM tasseled cap: *IEEE Transactions on Geosciences and Remote Sensing*, Vol. GE-22, No. 3, pp. 252–263.

Deer, P., 1995, *Digital Change Detection Techniques in Remote Sensing*: Defence Science and Technology Organisation Technical Report, p. 44.

Eguchi, R. T.; Gill, S. P.; Ghosh, S.; Svekla, W.; Adams, B. J.; Evans, G.; Toro, J.; Saito, K.; and Spence, R., 2010, The January 12, 2010, Haiti earthquake: A comprehensive damage assessment using very high resolution areal imagery. In *8th International Workshop on Remote Sensing for Disaster Management*: Tokyo Institute of Technology, Tokyo, Japan.

Eltahir, E. A. B., 1998, A soil moisture-rainfall feedback mechanism: *Water Resources Research*, Vol. 34, No. 4, pp. 765–776.

Felde, G. W.; Anderson, G. P.; Cooley, T. W.; Matthew, M. W.; Adler-Golden, S. M.; Berk, A.; and Lee, J., "Analysis of Hyperion data with the FLAASH atmospheric correction algorithm." Geoscience and Remote Sensing Symposium, 2003. IGARSS '03. Proceedings. 2003 IEEE International, vol. 1, no., pp.90, 92. vol. 1, 21-25 July 2013. Doi: 10.1109/IGARSS.2003.1293688

Gomberg, J. and Schweig, E., 2002, *East Meets Midwest: An Earthquake in India Helps Hazard Assessment in the Central United States*: U.S. Geological Survey Fact Sheet (FS-007-02).

Gupta, R. P., 2003, *Remote Sensing Geology*, 2nd ed.: Springer-Verlag, Heidelberg, 656 p.

Gupta, R. P.; Chander, R.; Tewari, A. K.; and Saraf, A. K., 1995, Remote-sensing delineation of zones susceptible to seismically induced liquefaction in the Ganga plains: *Journal of the Geological Society of India*, Vol. 46, No. 1, pp. 75–82.

Hisada, Y.; Shibayama, A.; and Ghayamghamian, M. R., 2005, Building damage and seismic intensity in Bam city from the 2003 Iran, Bam, earthquake, Bull. Earthquake Research Institute (ERI), 79, pp. 81–93.

Huang, C.; Wylie, B.; Yang, L.; Homer, C.; and Zylstra, G., 2002, Derivation of a tasselled cap transformation based on Landsat 7 at satellite reflectance: *International Journal of Remote Sensing*, Vol. 23, No. 8, pp. 1741–1748.

Huyck, C.; Adams, B.; Cho, S.; Chung, H. C.; and Eguchi, R., 2005, Towards rapid citywide damage mapping using neighborhood edge dissimilarities in very high-resolution optical satellite imagery—Application to the 2003 Bam, Iran earthquake: *Earthquake Spectra*, Vol. 21, No. S1, pp. 255–266.

Huyck, C.; Matsuoka, M.; Takahashi, Y.; and Vu, T., 2006, Reconnaissance technologies used after the 2004 Niigata-ken Chuetsu, Japan, earthquake: *Earthquake Spectra*, Vol. 22, pp. 133–145.

Jensen, J. R.; Cowen, D.; Narumalani, M.; and Halls, J., 1997, Principles of change detection using digital remote sensor data. In integration of Geographic Information Systems and Remote Sensing Star, J.L., Estes, J.E. and McGwire, K.C (Eds.), Cambridge University Press. Cambridge, pp. 37–54.

Kauth, R. J. and Thomas, G. S., 1976, The tasseled cap—A graphic description of the spectral temporal development of agricultural crops as seen in Landsat. In *Proceedings on the Symposium on Machine Processing of Remotely Sensed Data*: West Lafayette, Indiana, LARS, Purdue University, pp. 41–51.

Kayen, R.; Pack, R.; Bay, J.; Sugimoto, S.; and Tanaka, H., 2006, Ground-Lidar visualization of surface and structural deformation of the Niigata Ken Chuetsu, 23 October 2004, earthquake: *Earthquake Spectra*, Vol. 22, pp. 147–162.

Kohiyama, M. and Yamazaki, F., 2005, Damage detection for 2003 Bam, Iran, earthquake using Terra-Aster satellite imagery: *Earthquake Spectra*, Vol. 21, No. S1, pp. 267–274.

Lu, P. D.; Mausel, E. B.; and Moran, E., 2004, Change detection techniques: *International Journal of Remote Sensing*, Vol. 25, No. 12, pp. 2365–2407.

Mansouri, B.; Shinozuka, M.; Huyck, C.; and Houshmand, B., 2005, Earthquake-induced change detection in the 2003 Bam, Iran, earthquake by complex analysis using Envisat ASAR data: *Earthquake Spectra*, Vol. 21, pp. 275–284.

Matthew, M. W.; Adler-Golden, S. M.; Berk, A.; Richtsmeier, S. C.; Levine, R. Y.; Bernstein, L. S.; Acharya, P. K.; Anderson, G. P.; Felde, G. W.; Hoke, M. P.; Ratkowski, A., Burke, H. H.; Kaiser, R. D.; and Miller, D. P., 2000, Status of atmospheric correction using a MODTRAN4-bashed algorithm. Society of Photo-optical Instrumentation Engineers (SPIE) Proceeding, Algorithms for Multispectral, Hyperspectral, and Ultraspectral Imagery, VI -4049, pp. 199–207.

Mohanty, K.; Maiti, K.; and Nayak, S., 2001, *Change Detection Techniques*: GIS@Development, v3: Electronic document, available at http://www.gisdevelopment.net/

Mouat, D. A.; Mahin, G. C.; and Lancaster, J., 1993, Remote sensing techniques in the analysis of change detection: *Geocarto International*, Vol. 2, pp. 39–50.

Narula, P. L. and Choubey, S. K., 2001, *Macroseismic Surveys for the Bhuj (India) Earthquake of 26 January 2001*: Electronic document, available at http://www.iitk.ac.in/nicee/EQ_Reports/Bhuj/narula1.htm

Oommen, T. and Baise, L. G., 2010, Model development and validation for intelligent data collection for lateral spread displacements: *ASCE Journal of Computing in Civil Engineering*, Vol. 24, No. 6, pp. 467–477.

Oommen, T.; Baise, L. G.; and Vogel, R. M., 2010, Validation and application of empirical liquefaction models: *ASCE Journal of Geotechnical and Geoenvironmental Engineering*, Vol. 136, No. 12, pp. 1618–1633.

Oommen, T.; Baise, L. G.; and Vogel, R., 2011, Sampling bias and class imbalance in maximum likelihood logistic regression: *Mathematical Geosciences*, Vol. 43, No. 1, pp. 99–120.

Pandya, M. R.; Singh, R.; Murali, K. R.; Babu, P. N.; Kirankumar, A. S.; and Dadhwal, V. K., 2002, Bandpass solar exoatmospheric irradiance and Rayleigh optical thickness of sensors on board Indian remote sensing satellites-1B, -1C, -1D, and P4: *IEEE Transactions on Geoscience and Remote Sensing*, Vol. 40, No. 3, pp. 714–718.

Patel, P. P., 1997, *Ecoregions of Gujarat*: Gujarat Ecology Commission 163, GERI Campus, Race Course Road, Vadodara 390 007, India.

Prakash, A. and Gupta, R. P., 1998, Land-use mapping and change detection in a coal mining area—A case study in the Jharia coalfield, India: *International Journal of Remote Sensing*, Vol. 19, No. 3, pp. 391–410.

Prakash, A. and Gupta, R. P., 1999, Surface fires in Jharia coalfield, India—Their distribution and estimation of area and temperature from TM data: *International Journal of Remote Sensing*, Vol. 20, No. 10, pp. 1935–1946.

Prakash, A.; Sastry, R. G. S.; Gupta, R. P.; and Saraf, A. K., 1995, Estimating the depth of buried hot features from thermal IR remote sensing data—A conceptual approach: *International Journal of Remote Sensing*, Vol. 16, No. 13, pp. 2503–2510.

Rajendran, C. P. and Rajendran, K., 2001, Characteristics of deformation and past seismicity associated with the 1819 Kutch earthquake, northwestern India: *Bulletin of the Seismological Society of America*, Vol. 91, No. 3, pp. 407–426.

Ramakrishnan, D.; Mohanty, K. K.; Nayak, S. R.; and Chandran, R. V., 2006, Mapping the liquefaction induced soil moisture changes using remote sensing technique: An attempt to map the earthquake induced liquefaction around Bhuj, Gujarat, India: *Geotechnical and Geological Engineering*, Vol. 24, No. 6, pp. 1581–1602.

Rastogi, B. K., 2004, Damage due to the Mw 7.7 Kutch, India, earthquake of 2001: *Tectonophysics*, Vol. 390, No. 1–4, pp. 85–103.

Rathje, E. M. and Adams, B. J., 2008, The role of remote sensing in earthquake science and engineering: Opportunities and challenges: *Earthquake Spectra*, Vol. 24, No. 2, pp. 471–492.

Rathje, E. M.; Crawford, M.; Woo, K.; and Neuenschwander, A., 2005, Damage patterns from satellite images from the 2003 Bam, Iran, earthquake: *Earthquake Spectra*, Vol. 21, No. S1, pp. 295–307.

Rathje, E.; Kayen, R.; and Woo, K. S., 2006, Remote sensing observations of landslides and ground deformation from the 2004 Niigata Ken Chuetsu earthquake: *Soils and Foundations*, Vol. 46, No. 6, pp. 831–842.

Saraf, A. K.; Prakash, A.; Sengupta, S.; and Gupta, R. P., 1995, Landsat TM data for estimating ground temperature and depth of subsurface coal fire in the Jharia coalfield, India: *International Journal of Remote Sensing*, Vol. 16, No. 12, pp. 2111–2124.

Saraf, A. K.; Sinvhal, A.; Sinvhal, H.; Ghosh, P.; and Sarma, B., 2002, Satellite data reveals 26 January 2001 Kutch earthquake-induced ground changes and appearance of water bodies: *International Journal of Remote Sensing*, Vol. 23, No. 9, pp. 1749–1756.

Serpico, S. and Bruzzone, L., 1999, *Change Detection*: World Scientific Publishing, Singapore.

Shih, S. and Jordan, J., 1993, Use of Landsat Thermal-IR data and GIS in soil-moisture assessment: *Journal of Irrigation and Drainage Engineering*, Vol. 119, No. 5, pp. 868–879.

Singh, A., 1989, Digital change detection techniques using remotely sensed data: *International Journal of Remote Sensing*, Vol. 10, No. 6, pp. 989–1003.

Singh, R. P.; Bhoi, S.; and Sahoo, A. K., 2002, Changes observed in land and ocean after Gujarat earthquake of 26 January 2001 using IRS data: *International Journal of Remote Sensing*, Vol. 16, No. 23, pp. 3123–3128.

Srinivasulu, J. and Kulkarni, A. V., 2003, Estimation of spectral reflectance of snow from IRS-1D LISS-iii sensor over the Himalayan terrain: *Journal of Earth System Science*, Vol. 113, No. 1, pp. 117–128.

Vicente-Serrano, S.; Pons-Fernandez, X.; and Cuadrat-Prats, J., 2004, Mapping soil moisture in the Central Ebro River valley (northeast Spain) with Landsat and NOAA satellite imagery: A comparison with meteorological data: *International Journal of Remote Sensing*, Vol. 25, No. 20, pp. 4325–4350.

Warner, T. A. and Chen, X., 2001, Normalization of Landsat thermal imagery for the effects of solar heating and topography: *International Journal of Remote Sensing*, Vol. 22, No. 5, pp. 773–788.

Weather Underground, 2012, Weather Underground: Electronic document, available at http://www.wunderground.com/cgi-bin/findweather/hdfForecast?query=Bhuj+India

Yuan, D.; Elvidge, C.; and Lunetta, R. S., 1999, *Multispectral Methods for Land Cover Change Analysis*: Lunetta, R.S., Elvidge, C.D. (Eds), Remote Sensing Change Detection: Environmental Monitoring Methods and Applications. Tylor & Francis. London, pp. 21–39.

Yusuf, Y.; Matsuoka, M.; and Yamazaki, F., 2001, Damage assessment after 2001 Gujarat earthquake using Landsat-7 satellite images: *Journal of the Indian Society of Remote Sensing*, Vol. 29, No. 1, pp. 3–16.

Zhang, G.; Robertson, P.; and Brachman, R., 2004, Estimating liquefaction-induced lateral displacements using the Standard Penetration Test or Cone Penetration Test: *Journal of Geotechnical and Geoenvironmental Engineering*, Vol. 8, No. 130, pp. 861–871.